Sequential Small Coronal Mass Ejections Observed In situ and in White-Light Images by Parker Solar Probe

Brian E. Wood[1], Phillip Hess[1], Yu Chen[2], Qiang Hu[2,3]

ABSTRACT

We reconstruct the morphology and kinematics of a series of small transients that erupt from the Sun on 2021 April 24 using observations primarily from Parker Solar Probe (PSP). These sequential small coronal mass ejections (CMEs) may be the product of continuous reconnection at a current sheet, a macroscopic example of the more microscopic reconnection activity that has been proposed to accelerate the solar wind more generally. These particular CMEs are of interest because they are the first CMEs to hit PSP and be simultaneously imaged by it, using the Wide-field Imager for Solar Probe (WISPR) instrument. Based on imaging from WISPR and STEREO-A, we identify and model six discrete transients, and determine that it is the second of them (CME2) that first hits PSP, although PSP later more obliquely encounters the third transient as well. Signatures of these encounters are seen in the PSP in situ data. Within these data, we identify six candidate magnetic flux ropes (MFRs), all but one of which are associated with the second transient. The five CME2 MFRs have orientations roughly consistent with PSP encountering the right sides of roughly E-W oriented MFRs, which are sloping back towards the Sun.

Subject headings: Sun: coronal mass ejections (CMEs) — solar wind — interplanetary medium

1. Introduction

Parker Solar Probe (PSP) provides an opportunity to study coronal mass ejections (CMEs) closer to the Sun than ever before. However, the fraction of time PSP spends close to the Sun in its highly elliptical orbit is relatively small, and the odds of being hit by a CME during a particular perihelion passage are therefore relatively low. Thus, there are so far a limited number of events available for study during the 15 orbits that PSP has made around the Sun as of 2023 April. The most well-studied event dates back to the very first perihelion passage, where on 2018 November

[1]Naval Research Laboratory, Space Science Division, Washington, DC 20375, USA; brian.wood@nrl.navy.mil

[2]Center for Space Plasma and Aeronomic Research (CSPAR), The University of Alabama in Huntsville, Huntsville, AL 35805, USA

[3]Department of Space Science, The University of Alabama in Huntsville, Huntsville, AL 35805, USA

11 shortly after perihelion (2018 November 6) PSP encountered a CME while at a distance of 53 $R_\odot$ from the Sun (Korreck et al. 2020; Nieves-Chinchilla et al. 2020; Good et al. 2020). Other events observed in situ by PSP farther from the Sun have been analyzed by Winslow et al. (2021), Hu et al. (2022), and Möstl et al. (2022).

The PSP mission is primarily designed to study the solar wind and CMEs using a suite of on board particle and field detectors. However, PSP also possesses a white light imaging instrument, the Wide-field Imager for Solar Probe (WISPR) (Vourlidas et al. 2016). The two heliospheric imagers that consititute PSP/WISPR observe the solar wind in the ram direction of PSP's orbit, and are typically taking data only for about a month surrounding each perihelion. A number of CMEs have been observed by WISPR during these periods, dating back to the first orbit, with a small circular CME observed on 2018 November 1 (Hess et al. 2020; Rouillard et al. 2020), followed by a "streamer blob" event seen very near perihelion on 2018 November 5 (Wood et al. 2020). The transients studied so far have tended to be rather small and slow, but these images have still allowed CME structures to be seen in much greater detail than ever before (Liewer et al. 2020, 2021; Wood et al. 2021; Braga et al. 2022; Howard et al. 2022).

Given that WISPR observes in the direction of the spacecraft motion, WISPR sees transients passing in front of the spacecraft in its orbit, which are typically not hitting PSP. We report here on the first CME that both directly hits PSP and is imaged by WISPR while doing so, offering the first opportunity for WISPR and PSP's in situ instruments to be used to study the same CME. Unfortunately, this CME encounter is a complicated one, with WISPR observing many fronts passing through the field of view on 2021 April 24-25, just before PSP's eighth perihelion on April 29, with the spacecraft 46 $R_\odot$ from the Sun. Necessary clarity is provided by coronagraphic observations from STEREO-A, showing that the eruptive activity is more accurately described as a series of small CMEs erupting off the east limb, as viewed from STEREO-A's perspective. A central task of our analysis will be to utilize the WISPR and STEREO-A images to determine which of the small transients are actually hitting PSP, a necessary step toward properly interpreting the in situ signatures of the activity observed by PSP. There is also a prominence eruption associated with this activity, observed in EUV images from both STEREO-A and Solar Orbiter, but we refer the reader to Niembro et al. (2023) for a detailed discussion of the EUV data.

2. Observations

Although the principal stimuli of our analysis are the images and in situ observations from PSP on 2021 April 24-25, we first provide context for these data by presenting coronagraphic observations at that time from 1 au, in Figure 1. These images are from the COR2-A coronagraph on the STEREO-A spacecraft, which observes at angular distances from Sun-center of $0.7° - 4.2°$ $(2.5 - 15.6$ $R_\odot)$ (Howard et al. 2008). The images are displayed in a running-difference format, subtracting the previous image to emphasize the dynamic CME fronts. On 2021 April 24, COR2-A observes a series of small CMEs erupting off the east limb of the Sun. (The COR2-A observations of the activity are
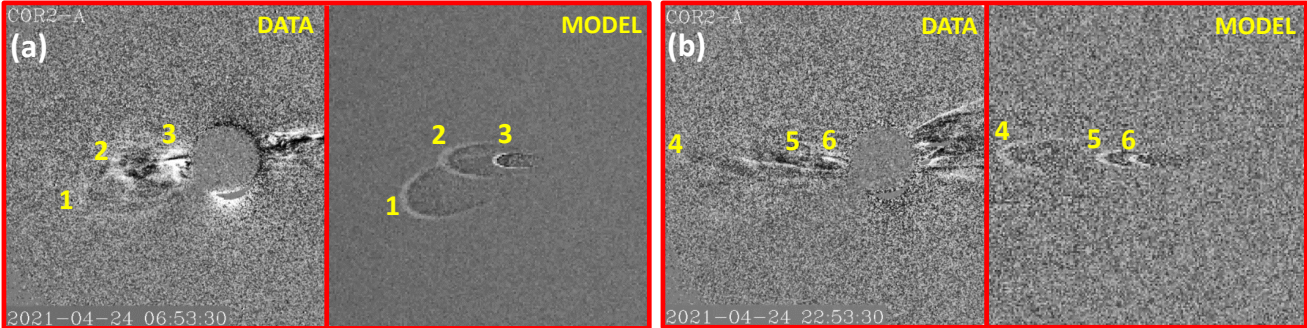
Fig. 1.— (a) On the left is an image of a series of three small CMEs (numbered 1-3) from UT 06:53:30 on 2021 April 24, taken by the COR2-A coronagraph on board STEREO-A. To the right of the image is a synthetic image based on the 3-D morphological reconstruction of the CMEs described in Section 3. The real and synthetic images are displayed in a running-difference format, and artificial noise is added to the synthetic image for aesthetic purposes. (b) Another COR2-A image, from UT 22:53:30 on 2021 April 24, showing three later small CMEs (numbered 4-6), with the synthetic model image again shown next to it. (A movie version of this figure is available in the online version of this article.)

covered more thoroughly in the movie version of Figure 1.) This sequence of transients is not easy to separate into distinct eruptions, but in Figure 1 we identify six separate little CMEs. Ideally, it would be preferable if it could be determined if there are truly separate magnetic flux rope (MFR) structures within these separate transients, to ensure these are in fact separate eruptions, but as will be discussed in more detail below, the available imaging data do not allow this to be clearly determined. This kind of sustained activity is not uncommon in coronagraphic data, and has been frequently observed by, for example, the Large Angle and Spectrometric COronagraph (LASCO) instrument on board the SOlar and Heliospheric Observatory (SOHO), which has been continously observing the Sun since 1996 (Brueckner et al. 1995). These CMEs are small enough that they could be considered in the category of "streamer blob" events (Sheeley et al. 1997; Wang et al. 1998).

Solar transients this small would normally not garner much attention, but in this instance the eruptions are directed right at PSP, making this our first opportunity to see what this kind of activity looks like up close. Figure 2 shows the locations of STEREO-A and PSP relative to Earth on 2021 April 24. It also explicitly shows the fields of view of the COR2-A coronagraph, and of PSP/WISPR's two heliospheric imagers: WISPR-I, imaging at $13° - 53°$ from the Sun, and WISPR-O, imaging at $50° - 108°$ (Vourlidas et al. 2016). Dashed lines in the figure indicate the central trajectories inferred for the six CMEs, based on the stereoscopic analysis that will be described in Section 3. The CMEs all pass very close to PSP, which is almost directly behind the Sun relative to Earth, explaining why SOHO/LASCO operating near Earth is unable to see any of this activity. As for STEREO-A imagery, the CMEs are observed by COR2-A, as shown in
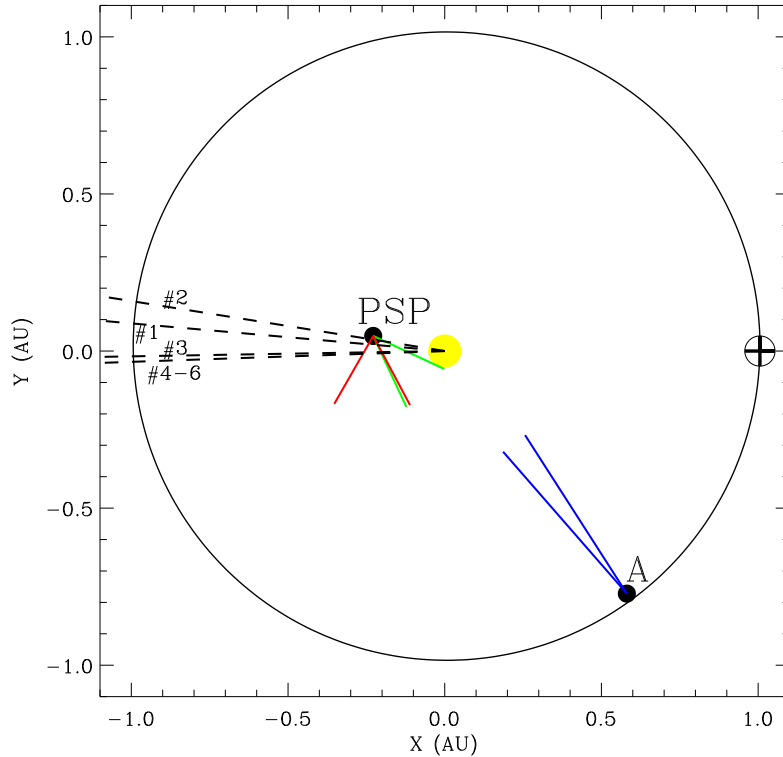
Fig. 2.— The positions of Earth, PSP, and STEREO-A in the ecliptic plane on 2021 April 24 (in HEE coordinates). At PSP's position, the green and red lines indicate the fields of view of the WISPR-I and WISPR-O detectors. At STEREO-A's position, the blue line indicates the field of view of COR2-A. The dashed lines indicate the central trajectories of six small CMEs observed by all these imagers.

Figure 1, but they are too faint to be discerned closer to the Sun by the COR1-A coronagraph; and the heliospheric imagers, HI1-A and HI2-A, are observing the wrong side of the Sun to view them. Thus, from STEREO-A we only have the COR2-A data. As noted in Section 1, there is a prominence eruption associated with this activity apparent in EUV imagery, but we refer the reader to Niembro et al. (2023) for a detailed analysis of those data, along with a discussion of potential signatures of the prominence in the PSP in situ data. We do note here that we see no clear evidence of the prominence in the white light images, which are naturally observing farther from the Sun than the EUV images.

In the WISPR images from 2021 April 24-25, a confusing series of fronts is observed passing through the field of view, as illustrated by two WISPR-I images in Figure 3. The movie version of this figure shows this more completely, and shows the WISPR-O imagery as well. The images are shown in an average-difference format, with an average WISPR-I image subtracted from the sequence. This activity is clearly associated with the sequence of transients seen by COR2-A in Figure 1, but connecting the WISPR-I fronts with the individual small COR2-A CMEs is nontrivial.
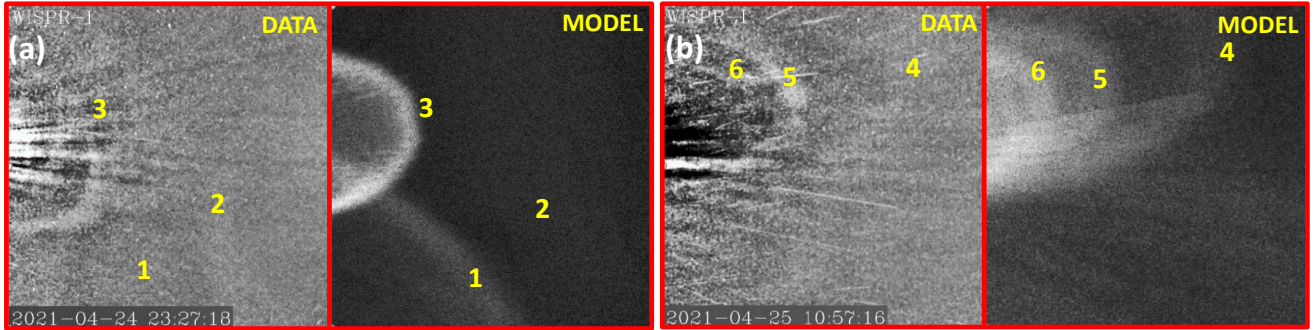
Fig. 3.— (a) On the left is a PSP/WISPR-I image of a series of fronts (numbered 1-3) observed on UT 23:27:18 on 2021 April 24, associated with the three CMEs observed by COR2-A in Figure 1(a). To the right of the image is a synthetic image based on the 3-D morphological reconstruction of the CMEs described in Section 3. The real and synthetic images are displayed in a average-difference format, and artificial noise is added to the synthetic image for aesthetic purposes. (b) Another WISPR-I image, from UT 10:57:15 on 2021 April 25, showing three later fronts (numbered 4-6), corresponding to the COR2-A CMEs seen in Figure 1(b), with the synthetic model image again shown next to it. (A movie version of this figure is available in the online version of this article, which also includes imagery from WISPR-O as well as WISPR-I.)

The numbers in Figure 3 indicate what fronts we ultimately associate with each CME in Figure 1. We will be referring to these CMEs using these numbers throughout the rest of this article.

The first transient, CME1, is noticeably south of the ecliptic in Figure 1, and is therefore identifiable in WISPR-I as a front only seen in the bottom third of the images from about UT 14:27–22:27. The other transients, starting with CME2, are all very close to the ecliptic plane. In the WISPR-I images, CME2 is seen as a very broad, very faint front passing rapidly through the field of view at UT 21:57–23:57, angled diagonally from the upper left to the lower right side of the images. As will be shown explicitly in the 3-D reconstruction described below in Section 3, this is what a CME front is expected to look like when directly hitting the spacecraft, and it is CME2 that we infer to be the first to impact PSP. The third transient, CME3, is the brightest in COR2-A, as shown most clearly in the movie version of Figure 1. We connect it with the bright, semicircular WISPR-I front seen clearly in Figure 3, which is the first of a series of similar looking fronts seen by WISPR-I, the most distinct of which we connect with the CME4-CME6 sequence of transients, which are particularly small and jet-like in COR2-A.

We have not described the WISPR-O images much (see movie version of Figure 3), as these data are even harder to interpret than the WISPR-I images. The detailed reconstruction of the eruptions described in the next section provides some clarity. From this it is clear that CME1 is not seen by WISPR-O at all, being too far south; CME2 is responsible for a bright, very broad front passing through the field of view at the end of April 24, oriented diagonally through the field of view (as in WISPR-I); CME3 is a large semi-circular front filling the field of view and

passing rapidly through it from about UT 4:34–6:34 on April 25; and the final three CME4–CME6 transients are only partially seen along the top of the WISPR-O field of view starting at about UT 11:34, and are hard to separate.

3. Three Dimensional Reconstruction of the Six CMEs

Modeling a CME's appearance in images requires both a morphological analysis, where the 3-D shape of the CME is approximated; and a kinematic analysis, where the Sun-center distance and speed of the CME's leading edge as a function of time are determined. We first discuss the kinematic component. For each CME, this begins with measurements of the elongation angle of the leading edge from Sun-center, ϵ, which then must be converted to actual distances from Sun-center, r, using some geometric approximation. A kinematic model can then be inferred from these r values.

In past analyses, we have usually focused on measurements from one spacecraft, with the choice of spacecraft based on which provides the best vantage point and/or the most extensive set of measurements covering the widest range of distances (e.g., Wood et al. 2017). However, a single spacecraft approach does not work in this case, because we only have data from two sources, STEREO/COR2-A and PSP/WISPR, which are observing the CMEs at different distances from the Sun, with no overlap. Thus, we combine ϵ measurements from both COR2-A and WISPR, and infer r from both. In practice, we only consider WISPR-I from PSP, as for most of the CMEs WISPR-O is only seeing parts of the CME fronts, with the leading edge not clearly in the field of view. (The only clear exception would be CME3.) Even for WISPR-I, meaningful measurements are not possible for CME1 or CME2. For CME1, the leading edge is below the WISPR-I field of view, and with CME2 directly hitting the spacecraft, PSP is not able to view its leading edge well.

The elongation angle measurements are shown in Figure 4(a) for the six CMEs. Converting ϵ to r requires a geometric approximation. The simplest one that is commonly used is the "Fixed-ϕ" approximation, which assumes the CMEs are narrow enough for their leading edges to be considered point-like, in which case

$$r = \frac{d \sin \epsilon}{\sin(\epsilon + \phi)}, \tag{1}$$

where d is the distance from the observer to the Sun and ϕ is the angle between the CME trajectory and the observer's line of sight to the Sun (Kahler & Webb 2007; Sheeley et al. 2008). Alternatively, if the CME front is approximated as a sphere centered halfway between the Sun and the leading edge, one finds

$$r = \frac{2d \sin \epsilon}{1 + \sin(\epsilon + \phi)}, \tag{2}$$

which has been called the "Harmonic Mean" approximation (Lugaz et al. 2009). More complicated relations exist (e.g., Davies et al. 2013), but we will only consider the Fixed-ϕ and Harmonic Mean assumptions here. It should be noted that the trajectory directions quantified by ϕ and shown
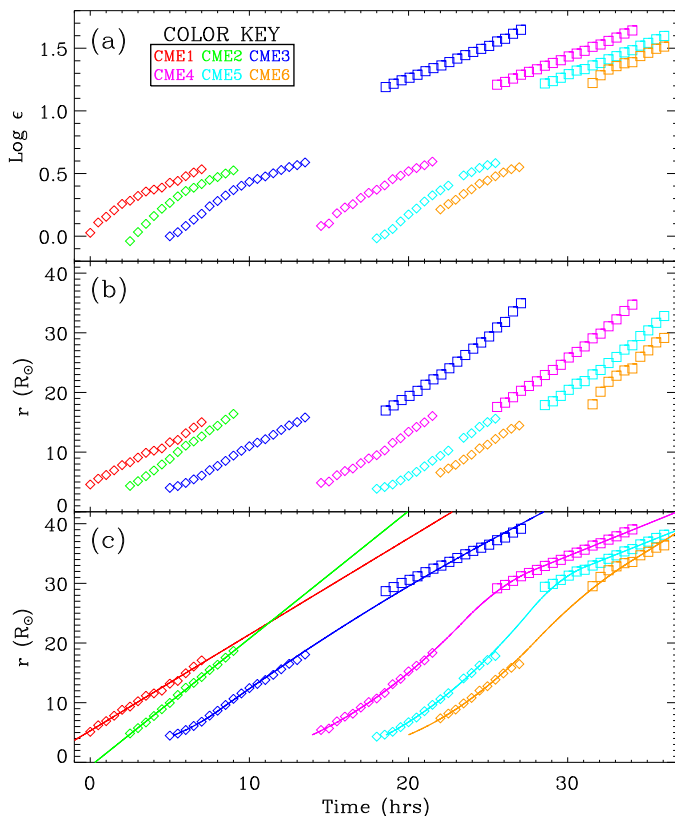
Fig. 4.— (a) Logarithmic elongation angles (ϵ, in degrees) are plotted versus time for the leading edges of each of the six CMEs observed on 2021 April 24–25. The $t = 0$ reference time is UT 01:23:30 on April 24. Diamonds are STEREO COR2-A measurements, and squares are from PSP/WISPR-I. (b) Sun-center distances, r, computed from ϵ assuming the Harmonic Mean approximation. Note the severe discontinuity between the COR2-A and WISPR-I measurements for CME3–CME6. (c) Sun-center distances computed assuming the Fixed-ϕ approximation, with better COR2-A/WISPR-I agreement. Simple kinematic models are fitted to the data (see text).

explicitly in Figure 2 are determined by the morphological part of the analysis described below. In practice, the generation of a full CME reconstruction involves iteration between the kinematic and morphological components of the analysis.

Figures 4(b) and 4(c) show the r measurements that result when the Harmonic Mean and Fixed-ϕ approximations are used, respectively. It is immediately clear that the results are poor for the Harmonic Mean option. The distances inferred from the WISPR measurements are too low relative to those inferred from COR2-A. The situation is improved when Fixed-ϕ is assumed. Although a more modest discontinuity still clearly exists, the implied kinematic profile seems more reasonable, with the higher inferred WISPR distances.

In a survey of 28 Earth-directed CMEs well observed by STEREO, both Harmonic Mean and Fixed-ϕ were considered (Wood et al. 2017), and in all but four cases it was the Harmonic

Table 1: CME Parameters

Parameter	Description	CME1	CME2	CME3	CME4	CME5	CME6
V_{COR2A} (km/s)	COR2-A speed	312	415	323	363	376	366
V_{WISPR} (km/s)	WISPR-I speed	...	...	233	222	225	274
λ_s (deg)	Trajectory longitude	175	171	181	182	182	182
β_s (deg)	Trajectory latitude	-12	0	0	1	1	1
$FWHM_s$ (deg)	Angular width	29	25	25	15	15	15
α_s	Leading edge shape	2.5	2.0	2.0	2.0	2.0	2.0

Mean approximation that was deemed better at providing a reasonable kinematic profile that yielded correct Earth arrival times and synthetic images that collectively best matched the multi-viewpoint data. However, those CMEs are bigger events than the narrow transients being modeled here. Because the 2021 April 24 CMEs are small and narrow, it is ultimately not surprising that Fixed-ϕ does better in this particular instance, given that the Fixed-ϕ approximation assumes a very narrow transient morphology.

Following past analyses (e.g. Wood et al. 2017), we fit a simple multi-phase kinematic model to the r measurements in Figure 4(c), with each phase corresponding to either a time of constant velocity or constant acceleration. Full kinematic models such as this allow synthetic images of CMEs to be computed for any time whatsoever after CME initiation, including times without r measurements (e.g., WISPR-O image times, or WISPR-I image times for CME1 and CME2). The resulting fits are represented as solid lines in the figure. For CME1 and CME2, where we only have COR2-A measurements, we simply use a single phase model assuming a constant velocity. It is fortunate that this ultimately leads to synthetic images that reproduce the actual images reasonably well (see below), which it should be mentioned would not be the case for CME3–CME6, which require the WISPR r constraints.

For CME3–CME6, we assume a three-phase model, with a period of constant acceleration followed by a period of constant deceleration, and finally a period of constant velocity. We have used this kind of model for many past CMEs (e.g., Wood & Howard 2009), in general representing the acceleration phase of a fast CME, a gradual deceleration as the CME is slowed by interaction with the slower ambient wind, and finally a constant velocity as the terminal CME speed is reached. In this case, the meaning of the inferred acceleration and deceleration phases is more ambiguous, as the fit will be using the acceleration to try to account for the aforementioned discontinuity between the COR2-A and WISPR-I measurements. For this reason, we do not bother to show the velocity profiles that correspond to the fits in Figure 4(c).

However, in the first two rows of Table 1, we list mean velocities observed for each of the CMEs in the COR2-A and WISPR-I fields of view, computed from simple linear fits to the COR2-A and WISPR-I height-vs-time data points. It is noteworthy that for CME3–CME6 we infer significantly lower velocities in WISPR-I than for COR2-A. Although systematic uncertainties in this analysis are high, we believe these decelerations are probably real, at least qualitatively, as they can be

explained as a natural consequence of these later CMEs plowing into the slower trailing parts of CME1 and CME2.

Turning our attention to the morphological part of the analysis, we rely on techniques used many times in the analysis of stereoscopic CME imaging, dating back to Wood & Howard (2009), but more thoroughly described by Wood et al. (2017). This is a forward modeling approach, involving the use of a parametrized functional form for the assumed CME shape, with the parameters adjusted to yield synthetic images that best match the observations. Synthetic image calculation includes full computation of the Thomson scattering from the model structure, although we only place mass on the surface of the structure to outline its shape. We are not here attempting to reproduce image brightnesses or measure CME masses, so the densities assumed at the surface are arbitrary. A popular paradigm for CME structure is that of a magnetic flux rope (MFR), i.e. a tube shape permeated with a helical magnetic field with both legs streching back toward the Sun, so we have usually assumed an MFR shape in 3-D CME reconstructions (Wood & Howard 2009). However, for the small, faint CMEs studied here, we really only perceive the transients as narrow fronts, with nothing to suggest the presence or orientation of an MFR. Thus, we instead assume here a simple lobular front shape, a prescription we have generally used in the past to model CME shocks, when visible ahead of the ejecta (e.g., Wood & Howard 2009; Wood et al. 2017), but which has also been used before to model the ejecta itself in other cases where an MFR shape is not clearly apparent (Wood et al. 2009).

Figure 5 shows the resulting model CME fronts, and their positions relative to each other and to PSP. The parameters used to define the fronts are listed in the last four rows of Table 1. The trajectory longitude and latitude of the CMEs are λ_s and β_s, respectively, based on a heliocentric Earth ecliptic (HEE) coordinate system, with the positive x-axis pointed toward Earth, and the positive z-axis pointed toward ecliptic north. The CME longitudes are shown explicitly in Figure 2, which are within $11°$ of each other. Only CME1 has a latitude significantly out of the ecliptic ($\beta_s = -12°$). The ϕ trajectory angles relative to STEREO-A and PSP used in equations (1) and (2) above can be computed from λ_s, β_s, and the known spacecraft positions. The α_s parameter in Table 1 defines the shape of the leading edge, with higher values of α_s being flatter and lower values being more rounded (see, e.g., Wood et al. 2017).

The widths of the CME fronts are quantified in Table 1 as a full-width-at-half-max, $FWHM_s$. The CMEs are all very narrow, with $FWHM_s$ ranging from $15°$ for CME4–CME6 to $29°$ for CME1. These values can be crudely compared with the widths inferred for CMEs modeled with MFRs, with $FWHM_s$ in those cases defining the width of the CME in the plane of the MFR. In the survey of 28 Earth-directed CMEs of Wood et al. (2017), the narrowest CME had $FWHM_s = 41.5°$. Even the tiny streamer blob CME observed by PSP/WISPR in 2018 November 5 had $FWHM_s = 43.6°$ (Wood et al. 2020). All this emphasizes that we are not perceiving much lateral extent for the small 2021 April 24 CMEs compared to past CMEs that we have studied stereoscopically.

The CME trajectories and morphological parameters were determined by a trial and error
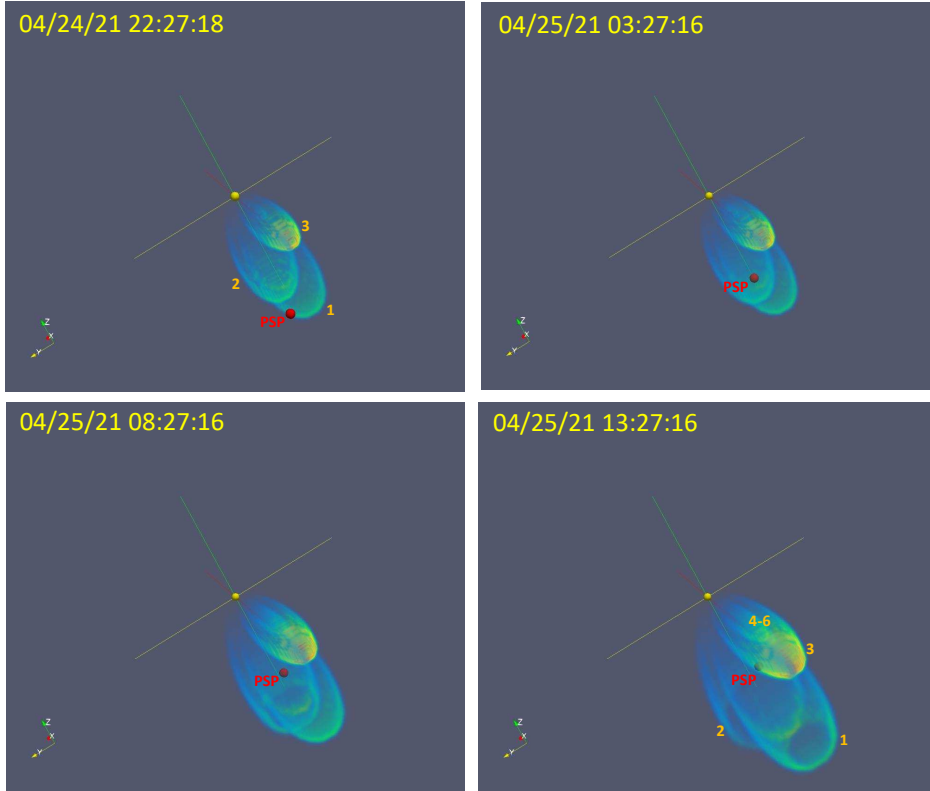
Fig. 5.— Three dimensional visualizations of the six reconstructed CME fronts, for four different times. The fronts are displayed in an HEE coordinate system, with the size of the Sun shown to scale in the figures. The time-dependent location of PSP is shown as a small red sphere. The first two frames show the positions of the first 3 CMEs (CME1–CME3) before and after CME2 hits PSP, respectively. The final frame shows PSP entering the flank of CME3. The last 3 very narrow CMEs (CME4-CME6) are buried inside CME3, as labeled in the final frame.

process of experimenting with different parameters to see which parameters lead to synthetic images that best match the real data. The self-similar expansion of the model CME fronts is defined by the kinematic models in Figure 4(c). The synthetic images resulting from our best-fit models are compared with the real images in Figures 1 and 3, with the movie versions of these figures available in the online article providing a more thorough comparison. Artificial noise is added to the synthetic images for aesthetic purposes. The added noise level is the same in absolute terms in all the images. The apparent lower noise in Figure 1(a) compared to 1(b) is illusory due to the upper range of the color scale being extended upwards to match the range of CME3, which is the brightest of the six CMEs.

It is difficult to estimate uncertainties in the parameters listed in Table 1. There have been many attempts to estimate errors in CME reconstructions based on multi-spacecraft imaging. A recent example is Verbeke et al. (2023), which also summarizes much of the past work on the subject. A lot of this work focuses on kinematic uncertainties, due to the interest in predicting

1 au arrival times at Earth for CMEs (e.g., Kilpua et al. 2012; Mays et al. 2015; Wood et al. 2017; Wold et al. 2018; Paouris et al. 2021), but morphological uncertainties are studied as well (e.g., Thernisien et al. 2009; Mierla et al. 2010; Jang et al. 2016; Balmaceda et al. 2018). Uncertainties in an analysis of this nature will depend greatly on the characteristics of the particular event in question, and on the particular viewing geometry for that event. The applicability of these studies to the very unique viewing geometry of the 2021 April 24 events directed right at PSP is unclear.

One characteristic of our reconstruction that is worthy of note is that the synthetic WISPR images are remarkably sensitive to the assumed trajectory direction, with shifts of only a degree or two making noticeable changes to the images. This is simply due to the extreme close proximity of the CMEs to the spacecraft (see Figure 2). Perhaps the best examples of this are the latitude parameters for CME3–CME6. For CME3, we infer $\beta_s = 0°$, while for CME4–CME6 we infer $\beta_s = 1°$. Such a small difference would usually not be significant in a CME reconstruction of this nature, but in this case it is significant. This is best indicated by the WISPR-O data, where the CME3 front is fully visible in the WISPR-O field of view, but the CME4–CME6 fronts are at least halfway above the field of view. Only a single degree of latitude shift in the reconstruction is enough to reproduce this.

With the image-based CME reconstruction now complete, we can finally address the central question of which CMEs are responsible for the in situ signatures observed by PSP. Our conclusions are illustrated by the four time frames shown in Figure 5. The first CME, CME1, is directed south of the ecliptic ($\beta_s = -12°$) and therefore does not hit PSP. It is CME2 that makes a direct hit to PSP at the end of April 24. The final panel of Figure 5 then shows PSP encountering the flank of CME3, with PSP's orbital motion being partly responsible for carrying the spacecraft into CME3, in addition to the expansion of the CME itself. The last three CMEs, CME4-6, are highly blended by the time they reach the vicinity of PSP. It is likely that PSP encounters trailing parts of these little transients near the beginning of April 26.

4. Comparison with PSP In-Situ Data

We will now compare the predictions of our image-based event reconstruction with measurements from PSP's plasma and field instruments, in order to see if the in situ data provide support for the reconstruction. The in situ data are shown in Figure 6. The proton density, velocity, and temperature measurements are from the Solar Wind Electrons Alphas & Protons (SWEAP) instrument on PSP (Kasper et al. 2016), while the magnetic field measurements are from the FIELDS instrument (Bale et al. 2016).

Vertical dashed lines in Figure 6 indicate when the 3-D reconstruction has PSP being hit by CME2 and CME3, the first right at the end of April 24, and the second midway through April 25. The PSP in situ data broadly support these predictions. The predicted CME2 encounter time corresponds to a substantial increase in velocity, magnetic field, and temperature. Proton
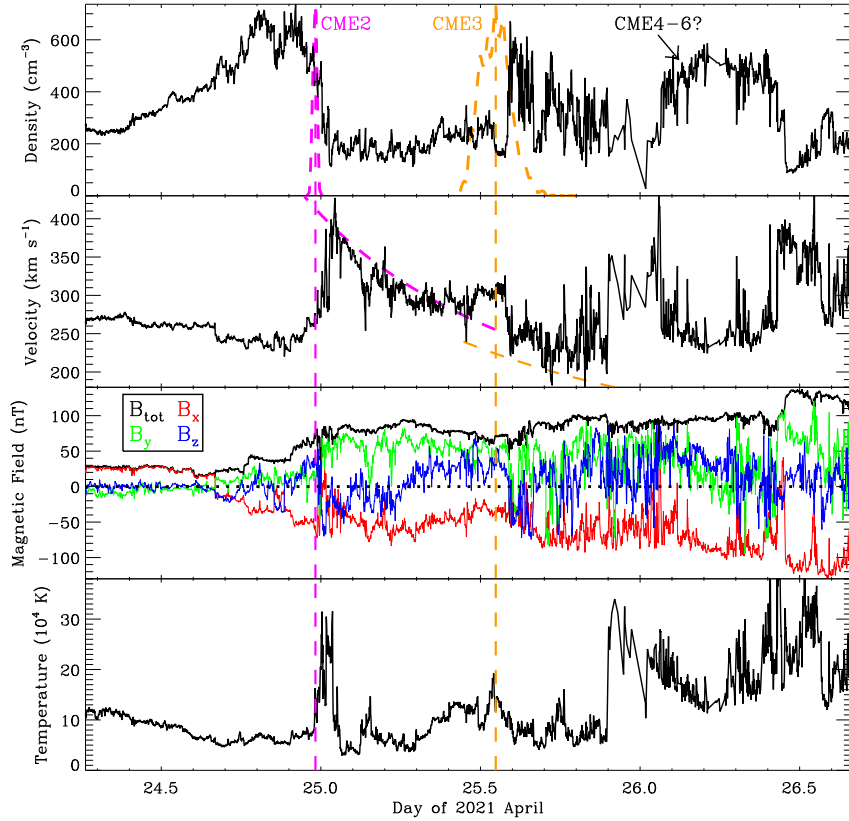
Fig. 6.— Plasma and field measurements from PSP/SWEAP and PSP/FIELDS during the passage of the 2021 April 24 transients over the spacecraft. The top two panels are proton number density and velocity. The third panel is the magnetic field at PSP, both the total field and the B_x, B_y, and B_z coordinates in an RTN coordinate system. The final panel is the proton temperature. Vertical dashed lines indicate the arrival times of CME2 and CME3 predicted by the 3-D reconstruction in Figure 5, and the density and velocity profiles predicted by this reconstruction are explicitly shown as well. The velocity profiles match the data well. The 3-D reconstruction implies that the broad density increase early in April 26 may be due to the last 3 modeled transients, CME4-6.

densities actually show a broad peak ahead of this arrival time, suggesting a pile-up region ahead of the CME. Possible signatures of the predicted CME3 encounter are more subtle, but there is a significant density increase at that time, along with a velocity decrease, and a modest temperature peak.

We do not try to show predicted encounter times for CME4-6, because these last three little transients are rather blended and are predicted to have an extended grazing incidence encounter with PSP, making predictions more uncertain. However, we do note in Figure 6 the existence of a broad density peak during the first half of April 26, which would correspond to the time when we would expect PSP to be affected by the passage of CME4-6.

The density and velocity profiles predicted at PSP for CME2 and CME3 by our 3-D recon-

struction are explicitly shown in the top two panels of Figure 6. The predicted velocity profiles indicate decreasing velocity behind the CME arrival, characteristic of self-similar expansion. These predictions agree well with the PSP/SWEAP observations, particularly for CME2. This is encouraging, considering the difficulties in deriving accurate kinematic models for these events (see Section 3).

A precise replication of the observed density profile is not expected, considering the very rudimentary density distribution assumed in the reconstruction, with mass placed only on the surfaces of the CME fronts. Gaussian density profiles across the surface are assumed, so the predicted PSP density profiles are roughly Gaussian as well. For CME2 the predicted profile is very narrow, indicative of the direct hit of CME2 on PSP, carrying PSP quickly through the CME surface. In contrast, the predicted density profile for CME3 is broad, as PSP enters CME3 with more of a grazing incidence (see last panel of Figure 5).

As for the magnetic field behavior, before the transients arrive PSP sees a positive-polarity Parker spiral behavior, with positive B_x and much weaker negative B_y. This changes in the pile-up region ahead of CME2, with B_x and B_y reversing sign, and the overall field strength increasing dramatically as CME2 arrives at the end of April 24. However, after CME2's arrival, the field behavior remains relatively consistent, despite the passages of the later transients. Throughout this period, B_x remains consistently negative and B_y generally positive.

One obvious thing to do with the in situ data is to look for evidence of MFRs, as it is generally assumed that MFRs lie at the hearts of all CMEs (Vourlidas et al. 2013). We have already noted that for these small, relatively faint CMEs, we perceive the transients in the white light images as simple lobular fronts, with no clear evidence of an MFR shape, but this does not preclude the existence of undetectable MFRs behind the visible leading fronts. However, the in situ data do not show obvious "magnetic cloud" signatures, which are considered the clearest indication of an MFR; with smoothly rotating, strong fields, low density, and low temperature (Burlaga et al. 1981; Marubashi 1986; Burlaga 1988; Lepping et al. 1990, 2015; Bothmer & Schwenn 1998). The absence of such a signature is particularly notable for CME2, for which our 3-D reconstruction implies a direct hit on PSP, which we would expect to yield an MFR signature in the in situ data, if an MFR is in fact present.

Nevertheless, there is field variability during the CME encounter, which could be indicative of distinct magnetic features that could be interpreted as MFRs. In order to explore this, we use an automated routine for finding MFRs within the solar wind, developed by Hu et al. (2018). Most MFRs found by this technique are quite small, with a median encounter duration of 20 minutes in *Wind* data. The basis of the routine is the Grad-Shafranov (GS) technique for inferring MFR orientations and deriving two-dimensional configurations for clear magnetic cloud events within in situ solar wind data (Hu & Sonnerup 2002; Hu 2017). Unlike more classic techniques for modeling such structures (e.g., Lepping et al. 1990, 2015; Nieves-Chinchilla et al. 2016), the GS methodology does not assume that the MFR has a symmetric circular or elliptical MFR cross section. The
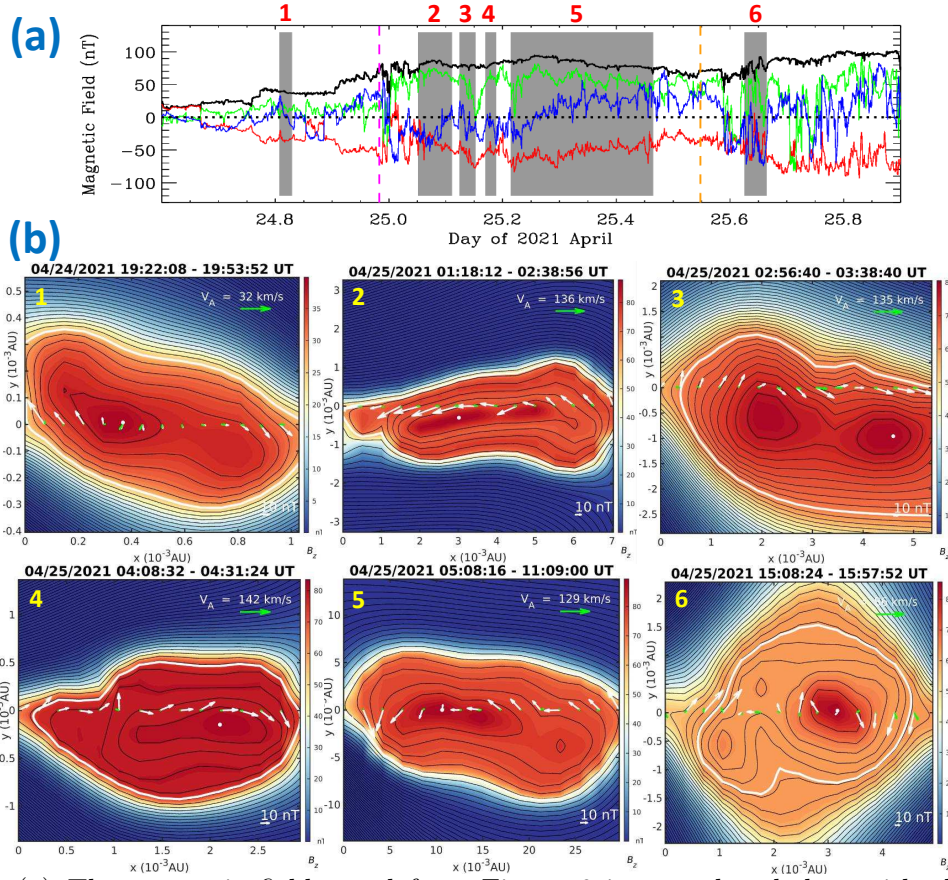
Fig. 7.— (a) The magnetic field panel from Figure 6 is reproduced, but with shaded regions indicating six intervals identified as possible MFRs by an automated routine (see Table 1). Vertical dashed lines indicate the arrival times of CME2 and CME3, as in Figure 6. (b) Grad-Shafranov reconstructed cross sections of the six MFRs. The color scale is the out-of-plane axial field in nT. The contours are the in-plane transverse magnetic field lines. The white and green arrows along $y = 0$ are the measured transverse field and remaining flow vectors, respectively, along the spacecraft path.

broader, more general theoretical requirements of the GS approach allows the automated Hu et al. (2018) MFR search routine to identify a greater number of potential MFR candidates within the solar wind than more restrictive techniques.

Hu et al. (2018) identified 74,241 small MFRs in *Wind* data from 1996–2016. Chen & Yu (2022) applied these techniques to PSP data from the first six PSP orbits, finding nearly 6000 MFRs. We now similarly apply the algorithm to our time interval of interest in 2021 April 24-26. Focusing only on longer candidates (≥ 20 min), we identify six possible MFR structures for which we can compute a full GS reconstruction. The time intervals of these MFRs are listed in Table 2 and displayed in Figure 7(a). The first MFR (MFR1) is in the pile-up region ahead of CME2's arrival at PSP based on the 3-D reconstruction. The next four MFRs are sequential within the

Table 2: Flux Rope Properties

MFR#	Start Time	Duration	Orientation		F_ϕ	F_ψ	F_ψ/F_ϕ
		(s)	ϕ (deg)	θ (deg)	(10^{10} Wb)	(10^{10} Wb)	
1	2021-04-24 19:22:08	1904	160	80	0.019	1.87	96.4
2	2021-04-25 01:18:12	4844	140	100	2.21	36.7	16.6
3	2021-04-25 02:56:40	2520	120	100	2.09	39.9	19.1
4	2021-04-25 04:08:32	1372	120	100	0.49	11.0	22.2
5	2021-04-25 05:08:16	21644	140	80	61.0	194	3.18
6	2021-04-25 15:08:24	2968	140	130	1.19	37.9	31.8

time period that we associate with the CME2 encounter. These four MFRs collectively account for most of that time period. The last of these (MFR5) is by far the largest, with an encounter duration of 6.0 hr. The final MFR (MFR6) is in the CME3 encounter period.

The full GS reconstructions of the six MFRs are shown in Figure 7(b), with a color scale that maps the axial field component of the MFR in the cross-sectional plane. In the GS modeling, the MFR is assumed to extend infinitely out of the plane in both directions, and the figures indicate the inferred spacecraft path through these structures along $y = 0$, projected into the cross-sectional plane. The orientation of the MFR is indicated by the ϕ and θ directions in Table 2, in the spacecraft-based RTN coordinate system. The ϕ angle indicates the azimuthal direction, with $\phi = 0°$ and $\phi = 180°$ pointed radially away and toward the Sun, respectively; while θ is the polar angle, with $\theta = 0°$ and $\theta = 180°$ pointed toward ecliptic north and south, respectively.

With $\theta = 80° - 100°$, the five CME2-associated MFRs are all oriented close to the ecliptic plane. With $\phi = 120° - 160°$, they are all encountered with the right side of the MFR slanted toward the Sun relative to the spacecraft-Sun line. Figure 8 explicitly shows the orientation of MFR5, with panel (b) showing how the MFR is tilted relative to the spacecraft's path in the ecliptic plane. With actual MFR structures assumed to have legs that stretch back toward the Sun, the inferred $[\phi,\theta]$ angles could be consistent with PSP encountering the right sides of roughly E-W oriented MFRs. However, it should be noted that the GS analysis assumes that the MFR extends infinitely in directions out of the cross-sectional plane. This introduces significant uncertainty in the interpretation of the MFR orientation angles on large scales. In the example of the large CME2 MFR (e.g., MFR5), significant curvature would be expected for it to be contained within the confines of the rather narrow CME outline defined by the CME lobular front inferred from the 3-D reconstruction.

Besides the MFR orientation information, Table 2 also provides estimates of the toroidal and poloidal magnetic fluxes of the GS-constructed MFRs, F_ϕ and F_ψ, respectively. The toroidal or axial flux is easiest to understand, as it is simply the magnetic flux through the cross-sectional plane illustrated in Figure 7 for each MFR. The poloidal flux is the integration of the azimuthal field around the central axis times the area of the surface through which this field is passing. This flux is much more uncertain than F_ϕ, since one must first assume that the azimuthal field times

(a)

View from +R direction
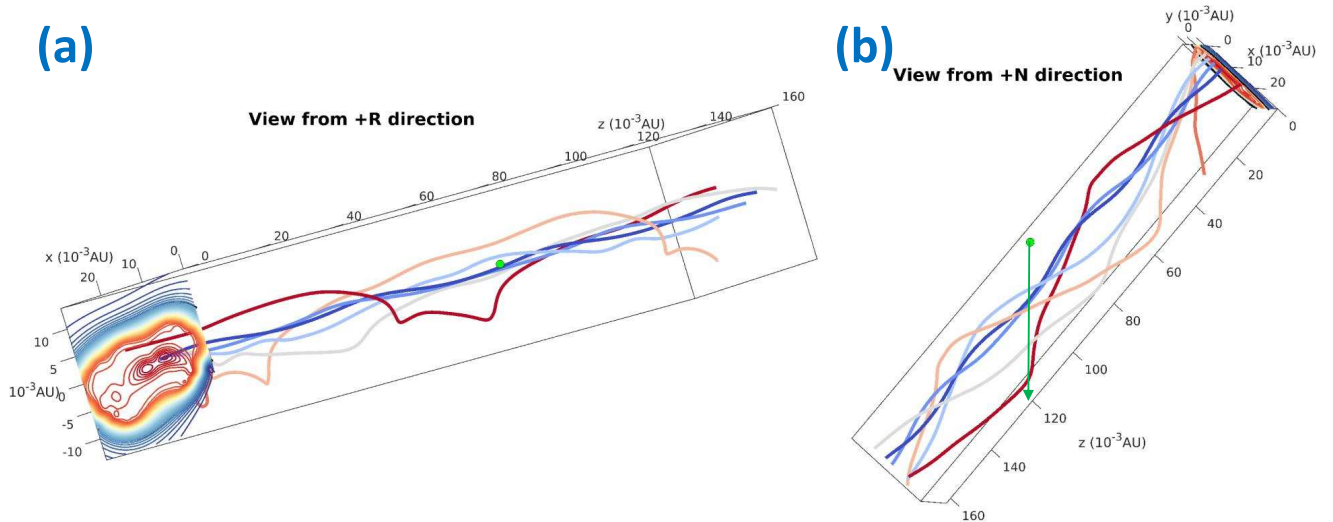
(b)

View from +N direction

Fig. 8.— (a) The 3-D magnetic field configuration of MFR5 (see Figure 7), viewed from a positive-R direction, looking toward the Sun, with the green dot indicating PSP's path through the structure. The field lines are traced from the cross-sectional map on the left. (b) Here MFR5 is viewed from a positive-N direction, looking down on the MFR with the Sun toward the bottom, and the green arrow indicating PSP's path through the MFR.

the MFR radius is unchanged along the MFR length (i.e., under a 2-D geometry), and also a total length of the MFR must be known or assumed. In principle, this could come from an image-based reconstruction of the MFR shape, but in this case the MFR shapes are not discerned in the images and we can only infer an outline of the CME leading edge. Still, we can use the length of the curve outlining the lobular fronts as our estimate for MFR length. At a distance from the Sun of 45 $R_\odot$, this length is 94.6 $R_\odot$ based on the CME2 front shown in Figure 5, so the F_ψ values in Table 2 are computed assuming this length. Finally, the last column of Table 2 lists the ratio of F_ψ to F_ϕ. These ratios are higher for the smaller MFRs.

5. Summary and Discussion

The 2021 April 24-25 event is the first CME that directly hits PSP and is simultaneously imaged by it. We have performed a full 3-D reconstruction of the event based on the available imagery, which unfortunately is limited to COR2-A and WISPR. The reconstruction is also complicated because the activity actually consists of multiple little CMEs erupting sequentially from the solar corona, but we have successfully connected six distinct, small CMEs seen by COR2-A near the Sun with fronts seen by WISPR-I and WISPR-O as the transients pass either over or very near PSP. The analysis clearly identifies CME2 as the transient that first impacts PSP directly, with PSP

later predicted to encounter CME3 more obliquely.

We have found support for the 3-D reconstruction from PSP in situ data, with density, temperature, and field signatures of the expected CME2 and CME3 impacts present in the in situ data. The declining velocity profiles observed in situ are also in excellent agreement with those predicted by the reconstruction, which simply assumes self-similar expansion. A broad density enhancement early in April 26 may be due to the collective influence of CME4-6.

Finally, we have used the GS-based automated MFR finding routine of Hu et al. (2018) to identify MFR candidates within the PSP encounter time, ultimately focusing on six of the longer candidates, all but the last associated with the CME2 encounter period. The fifth MFR is by far the largest, with an encounter duration of about 6 hours. The five CME2 MFRs have orientations roughly consistent with PSP encountering the right sides of roughly E-W oriented MFRs, which are sloping back towards the Sun.

The multiple eruptions seen by COR2-A are suggestive of intermittent reconnection occuring near the heliospheric current sheet, an interpretation consistent with the PSP in situ data showing a clear change in field polarity at the beginning of the CME encounter. Small-scale magnetic islands are commonly observed near current sheets (Khabarova et al. 2015), which could be interpreted as small MFR structures, and which are potential sources of particle acceleration (Zank et al. 2017; Van Eck et al. 2022). After initial formation, small MFRs are expected to merge into larger ones (Drake et al. 2021). It is possible that the sequence of CME2 MFRs in Figure 7 is indicative of such a process, with a large, dominant MFR (MFR5) preceded by much smaller MFRs that never merged with the large MFR before flowing away from the reconnection site.

It is becoming more popular to envision microscale interchange reconnection as being responsible for both the ubiquitous switchback structures observed by PSP (Drake et al. 2021), and potentially for the solar wind as a whole (Wang 2020; Raouafi et al. 2023). Activity such as the 2021 April 24-25 events may provide a way to study this important process on a more macroscopic scale, large enough for the intermittent outflows from such reconnection to be apparent in imaging. The 2021 April 24-25 events are potentially particularly useful for such purposes, with PSP providing both imaging and in situ observations close to the Sun. Thus, these data may be worthy of more detailed analysis in the future.

REFERENCES

Bale, S. D., Goetz, K., Harvey, P. R., et al. 2016, Space Sci. Rev., 204, 49

Balmaceda, L. A., Vourlidas, A., Stenborg, G., & Del Lago, A. 2018, ApJ, 863, 57

Bothmer, V., & Schwenn, R. 1998, Ann. Geophys., 16, 1

Braga, C. R., Vourlidas, A., Liewer, P. C., et al. 2022, ApJ, 938, 13

Brueckner, G. E., Howard, R. A., Koomen, M. J., et al. 1995, Sol. Phys., 162, 357

Burlaga, L. F. 1988, JGR, 93, 7217

Burlaga, L., Sittler, E., Mariani, F., & Schwenn, R. 1981, JGR, 86, 6673

Chen, Y., & Hu, Q. 2022, ApJ, 924, 43

Davies, J. A., Perry, C. H., Trines, R. M. G. M., et al. 2013, ApJ, 777, 167

Drake, J. F., Agapitov, O., Swisdak, M., et al. 2021, A&A, 650, A2

Good, S. W., Kilpua, E. K. J., Ala-Lahti, M., et al. 2020, ApJ, 900, L32

Hess, P., Rouillard, A. P., Kouloumvakos, A., et al. 2020, ApJS, 246, 25

Howard, R. A., Moses, J. D., Vourlidas, A., et al. 2008, Space Sci. Rev., 136, 67

Howard, R. A., Stenborg, G., Vourlidas, A., et al. 2022, ApJ, 936, 43

Hu, Q. 2017, Sci. China Earth Sci., 60, 1466

Hu, Q, He, W., & Chen, Y. 2022, Frontiers in Physics, 10, 960315

Hu, Q., & Sonnerup, B. U. Ö. 2002, JGR, 104, 6899

Hu, Q., Zhang, J., Chen, Y., le Roux, J., & Zhao, L. 2018, ApJS, 239, 12

Jang, S., Moon, Y. J., Kim, R. S., Lee, H., & Cho, K. S. 2016, ApJ, 821, 95

Kahler, S. W., & Webb, D. F. 2007, JGR, 112, A09103

Kasper, J. C., Abiad, R., Austin, G., et al. 2016, Space Sci. Rev., 204, 131

Khabarova, O., Zank, G. P., Li, G., et al. 2015, ApJ, 808, 181

Kilpua, E. K. J., Mierla, M., Rodriguez, L., et al. 2012, Sol. Phys., 279, 477

Korreck, K. E., Szabo, A., Nieves-Chinchilla, T., et al. 2020, ApJS, 246, 69

Lepping, R. P., Jones, J. A., & Burlaga, L. F. 1990, JGR, 95, 11957

Lepping, R. P., Wu, C. -C., Berdichevsky, D. B., & Szabo, A. 2015, Sol. Phys., 290, 2265

Liewer, P. C., Qiu, J., Penteado, P., et al. 2020, Sol. Phys., 295, 140

Liewer, P. C., Qiu, J., Vourlidas, A., Hall, J. R., & Penteado, P. 2021, A&A, 650, A32

Lugaz, N., Vourlidas, A., & Roussev, I. I. 2009, Ann. Geophys., 27, 3479

Marubashi, K. 1986, Adv. Space Res., 6, 335

Mays, M. L., Taktakishvili, A., Pulkinnen, A., et al. 2015, Sol. Phys., 290, 1775

Mierla, M., Inhester, B., Antunes, A., et al. 2010, Ann. Geophys., 28, 203

Möstl, C., Weiss, A. J., Reiss, M. A., et al. 2022, ApJ, 924, L6

Niembro, T., Seaton, D. B., Hess, P., et al. 2023, FrASS, in press

Nieves-Chinchilla, T., Linton, M. G., Hidalgo, M. A., et al. 2016, ApJ, 823, 27

Nieves-Chinchilla, T. N., Szabo, A., Korreck, K. E., et al. 2020, ApJS, 246, 63

Paouris, E., Vourlidas, A., Papaioannou, A., & Anastasiadis, A. 2021, Space Weather, 19, e02617

Raouafi, N. E., Stenborg, G., Seaton, D. B., et al. 2023, ApJ, 945, 28

Rouillard, A. P., Poirier, N., Lavarra, M., et al. 2020, ApJS, 246, 72

Sheeley, N. R., Jr., Herbst, A. D., Palatchi, C. A., et al. 2008, ApJ, 675, 853

Sheeley, N. R., Jr., Wang, Y. -M., Hawley, S. H., et al. 1997, ApJ, 484, 472

Thernisien, A., Vourlidas, A., & Howard, R. A. 2009, Sol. Phys., 256, 111

Van Eck, K., le Roux, J., Chen, Y., Zhao, L. L., & Thompson, N. 2022, ApJ, 933, 80

Verbeke, C., Leila Mays, M., Kay, C., et al. 2023, Adv. Space Res., in press (https://doi.org/10.1016/j.asr.2022.08.056)

Vourlidas, A., Howard, R. A., Plunkett, S. P., et al. 2016, Space Sci. Rev., 204, 83

Vourlidas, A., Lynch, B. J., Howard, R. A., & Li, Y. 2013, Sol. Phys., 284, 179

Wang, Y. -M. 2020, ApJ, 904, 199

Wang, Y. -M., Sheeley, N. R., Jr., Walters, J. H., et al. 1998, ApJ, 498, L165

Winslow, R. M., Lugaz, N., Scolini, C., & Galvin, A. B. 2021, ApJ, 916, 94

Wold, A. M., Mays, M. L., Taktakishvili, A., et al. 2018, JSWSC, 8, A17

Wood, B. E., Hess, P., Howard, R. A., et al. 2020, ApJS, 246, 28

Wood, B. E., Braga, C. R., & Vourlidas, A. 2021, ApJ, 922, 234

Wood, B. E., & Howard, R. A. 2009, ApJ, 702, 901

Wood, B. E., Howard, R. A., Thernisien, A., Plunkett, S. P., & Socker, D. G. 2009, Sol. Phys., 259, 163

Wood, B. E., Wu, C. -C., Lepping, R. P., et al. 2017, ApJS, 229, 29

Zank, G. P., Adhikari, L., Hunana, P., et al. 2017, ApJ, 835, 147